Estimation of a near-surface velocity anomaly from stacking velocities

John Toldi

INTRODUCTION

This paper examines a field dataset that shows strong lateral variation in the stacking velocities. By means of a linear theory (Loinger, 1983), these stacking velocities can be related to the underlying interval velocity model (the theory actually uses $slowness = \frac{1}{velocity}$). The paper begins with a brief review of the linear theory between interval-slowness anomalies and the corresponding stacking-slowness anomalies.

All of the reflectors in the field dataset have laterally varying stacking slownesses. The results of applying the linear theory to this dataset show that the cause of the lateral variation in stacking slowness is a near-surface, low-velocity (i.e. high slowness) zone. The validity of these results is confirmed by an analysis of the traveltimes predicted by the interval slowness model.

The linear theory

This method of velocity analysis is based on a separation of the interval velocity distribution into two parts: a background velocity distribution that is laterally invariant and a perturbation that contains the lateral variations. The linear theory relates the laterally-varying perturbation to the resulting stacking-slowness perturbations. This linear theory is briefly reviewed in the following two pages.

For a reflector at depth z_r, the linear theory provides the stacking slowness response as a function of midpoint y, to an impulse of anomalous interval slowness at position (y_{an}, z_{an}). More precisely,

$$\Delta w_s(y, z_r) = G(y, z_r, z_{an}, y_{an})\, \Delta w_{in}(y_{an}, z_{an})\, \Delta y_{an}\, \Delta z_{an} \tag{1}$$

where Δw_s , Δw_{in} and G are the anomalous stacking slowness, the anomalous interval slowness, and the impulse response respectively. The geometry is shown in figure 1.

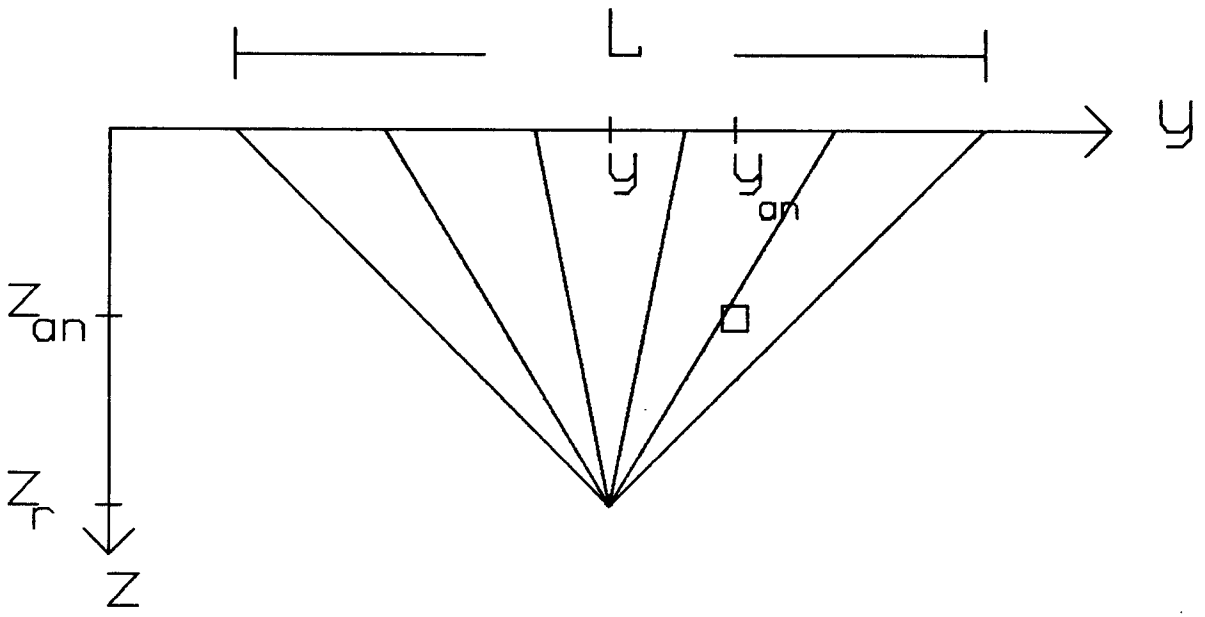

FIG. 1. Geometry for constant background velocity. Shown are a few raypaths to the reflector at depth z_r for the midpoint gather at y. The maximum offset is L. The impulse of anomalous interval slowness has coordinates (y_{an}, z_{an}).

For completeness I include the impulse response, G,

$$G(y, z_r, z_{an}, y_{an}) = \frac{15 z_r}{L^2 L'} \left[3 \left(\frac{2y}{L'} \right)^2 - 1 \right] \left[1 + \frac{L^2}{4z^2} \left(\frac{2y}{L'} \right)^2 \right] \qquad (2)$$

A full derivation of equation (2) can be found in Rocca and Toldi, 1982. $L' = effective\ cable\ length$, is defined in figure 2. As can be seen from figure 2, the stacking slowness at one midpoint will be influenced by interval slowness anomalies within half an effective cable length to either side. The effective cable length L' is thus the aperture of the filter that relates interval slowness to stacking slowness. For a constant background velocity,

$$L' = \frac{(z - z_{an})}{z} L$$

More generally, L' depends on the details of the maximum-offset raypath. Indeed, L' contains all of the information about the raypaths in a depth-variable background velocity.

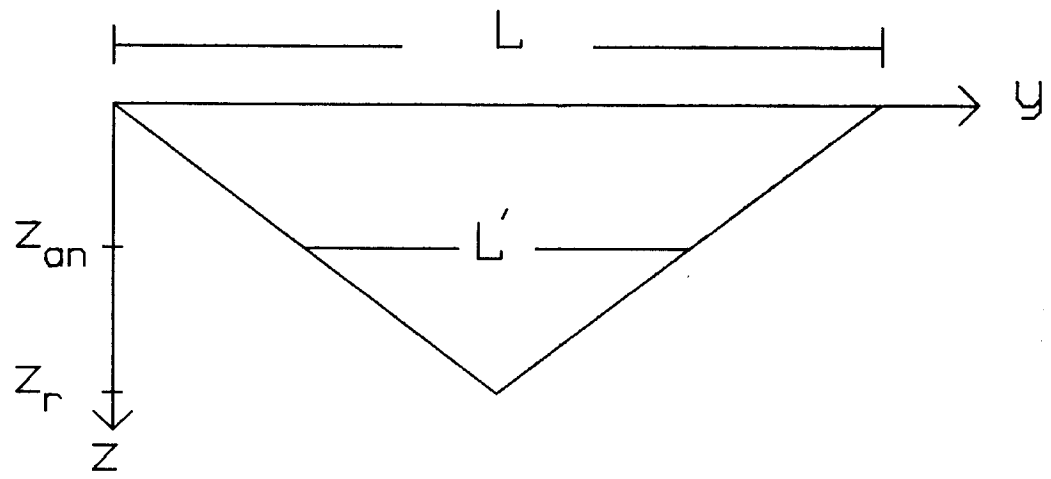

FIG. 2. L is the maximum offset, i.e. the cable length. L' is the effective cable length for reflector at depth z_r and anomaly at depth z_{an}.

Superposing the effects of impulses at all depths and midpoints, one finds:

$$\Delta w_s(z_r, y) = \int\int G(z_r, y, y_{an}, z_{an})\, \Delta w_{in}(y_{an}, z_{an})\, dy_{an}\, dz_{an} \tag{3}$$

Thus, the anomalous stacking slowness measured at midpoint y, for the reflector at depth z_r, is just the integral over the "fan" shown in figure 1. $G(z_r, y, y_{an}, z_{an})$ supplies a series of weights for this fan.

By expressing the interval slowness in terms of a set of basis functions $(h_j(y_{an}, z_{an}))$, one can convert the integral of equation (3) into a sum. Thus, with

$$\Delta w_{in}(y_{an}, z_{an}) = \sum_{j=0}^{n} w_j\, h_j(y_{an}, z_{an}) \tag{4}$$

equation (3) becomes

$$[\Delta w_s]_i = \sum_{j=0}^{n} G_{ij}\, w_j \tag{5}$$

where,

$$G_{ij} = \int\int G(z_r, y, y_{an}, z_{an})\, h_j(y_{an}, z_{an})\, dz_{an}\, dy_{an} \tag{6}$$

The subscript i refers to the point in the data space: each $[\Delta w_s]_i$ is the anomalous stacking slowness for a specific reflector at a specific midpoint. Treating the data as one big vector leads to the simple notation of equation (5).

Equation (5) can be inverted to produce an estimate of the anomalous interval slownesses. The work presented in this paper uses a generalized inverse formed by means of Singular Value Decomposition. Another paper in this report (Toldi, 1984) presents an alternate formulation of the velocity analysis problem that leads to an iterative construction of the inverse.

CALCULATING LATERALLY VARIABLE INTERVAL VELOCITIES

Data preparation

Figure 3 shows a stacked section for a seismic line recorded in the Central Valley of California. The data were stacked using one stacking velocity function for the entire line. The time sag, together with the reduction in the coherence beneath midpoint 125 indicate some kind of a near-surface low-velocity anomaly.

The low velocities are known to be caused by gas seeping upward from the zone around 2 seconds. Thus, although the data show some indication of a near-surface anomaly, the low-velocity zone could extend considerably deeper. This paper shows that the lateral variations in stacking velocity can be used to delineate this low-velocity zone.

The process begins with a data preparation step - a so-called horizon velocity analysis. This analysis provides stacking velocity (or in my case stacking slowness), as a function of midpoint for a chosen set of reflectors. Figure 4 shows the picked stacking-slowness curves for the reflectors at .5 seconds and 1.35 seconds.

These two reflectors provided stacking slownesses picks of comparable quality. Experiments using other shallow reflectors led to poorer results, particularly in the layers between the additional reflectors. This was probably due to picking errors; the stacking slownesses for these additional reflectors could only be picked with some difficulty.

Much of the problem with bad picks could be avoided by using a scheme that weights the datapoints according to their quality. Indeed, I show a weighting scheme in an accompanying paper that leads to excellent results. Nonetheless, the emphasis is still on shallow reflectors because of the short cable (maximum offset = 3600 feet) used in the recording of the data. Deeper reflectors have raypaths so near to vertical, that they provide little information about the depth of the anomaly.

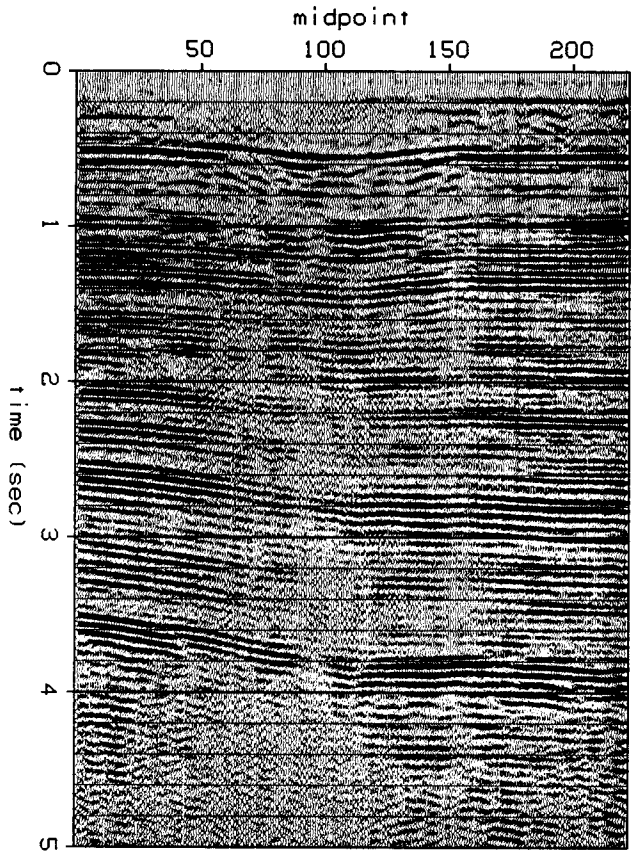

FIG. 3. CMP stack from Central Valley of California. One NMO velocity function was used for the entire line. Note the large time sag, and the reduction in coherence beneath midpoint 125.

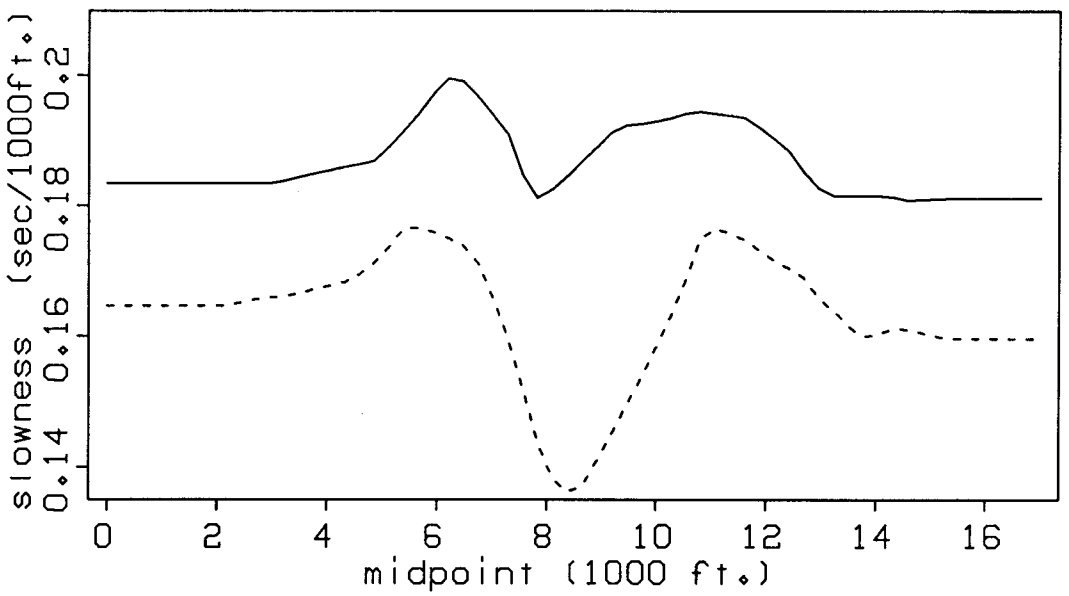

FIG. 4. Stacking slowness versus midpoint. Solid line: for reflector at .5 seconds. Dashed line: for reflector at 1.35 seconds.

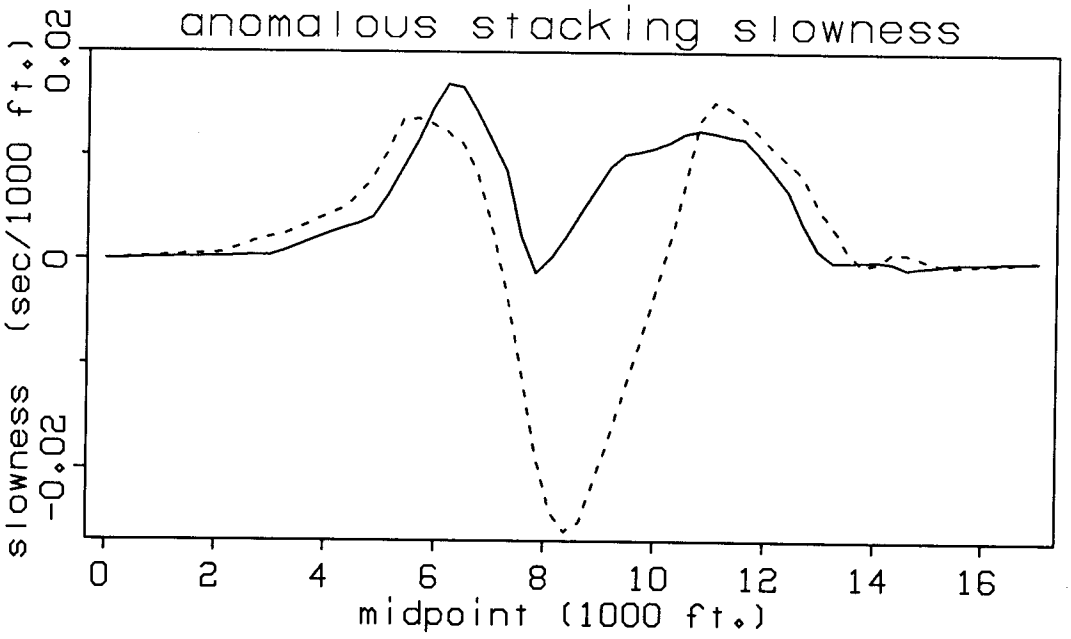

FIG. 5. Anomalous stacking slowness versus midpoint. Solid line: for reflector at .5 seconds. Dashed line: for reflector at 1.35 seconds.

The next step is to determine the anomalous part of the stacking slownesses, i.e. that part of the picked stacking slownesses not predicted by the background model. The background velocity is assumed to be laterally invariant. Thus, the Dix equation can be used to relate stacking velocity to interval velocities for this model, with the laterally invariant stacking velocities being just an average over the entire line. Subtracting off the contribution of the background leads to the two curves shown in figure 5. These two curves are the Δw_s used in equation (5).

Model space

To parameterize the model, I choose a suitable set of basis functions: thin strips in depth, and sinusoids laterally. Thus, the two controlling factors are the cutoff-wavenumber in the lateral direction, and the number of anomalous layers in depth. The examples shown here used a cutoff wavenumber with wavelength equal to twice the width of the Fresnel zone for the deeper reflector. To avoid truncation artifacts, I actually used a tapered cutoff in wavenumber.

The determination of residual statics could have been incorporated into the process, if a very thin, near-surface layer had been included in the model. This layer would need a spatial sampling much finer than the rest of the model. I feel that the short-wavelength component of the near-surface velocity can be better determined in a separate residual statics program, which makes full use of the surface consistency. Long-wavelength statics are, however, more intimately connected with velocity anomalies that extend to some depth; they are best treated as part of the velocity analysis. Thus, as a preprocessing step, I removed the effects of the short-wavelength component of the statics. The statics were determined using Shuki Ronen's statics program (Ronen, 1984).

Inversion results

The first example has nine anomalous layers; my goal was to resolve the depth of an anomaly to an increment less than the reflector separation. Figure 6 shows the anomalous interval slowness derived for this nine layer model. The damping factor was set at 7% (the ratio of damping factor to largest eigenvalue was $1/26 = .07$). The main feature is quite clear: there is a positive slowness anomaly (low-velocity) near the surface. Most of the lateral variation in interval velocity lies in the zone above the shallower reflector. Note that there was considerable lateral variation in the stacking slowness from the deeper reflector (see figure 5). Thus the method has attributed that variation to the near surface.

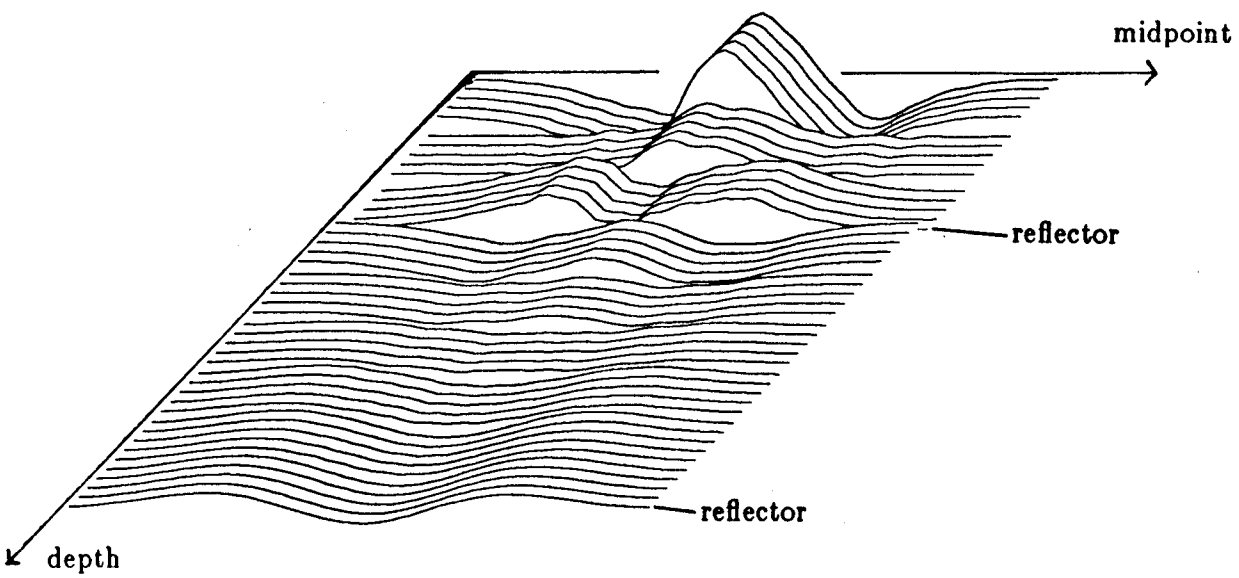

FIG. 6. Anomalous interval slowness model, derived for nine layer model. For display purposes the slowness in each layer is repeated five times; thus the discrete nature of the model in depth is clear.

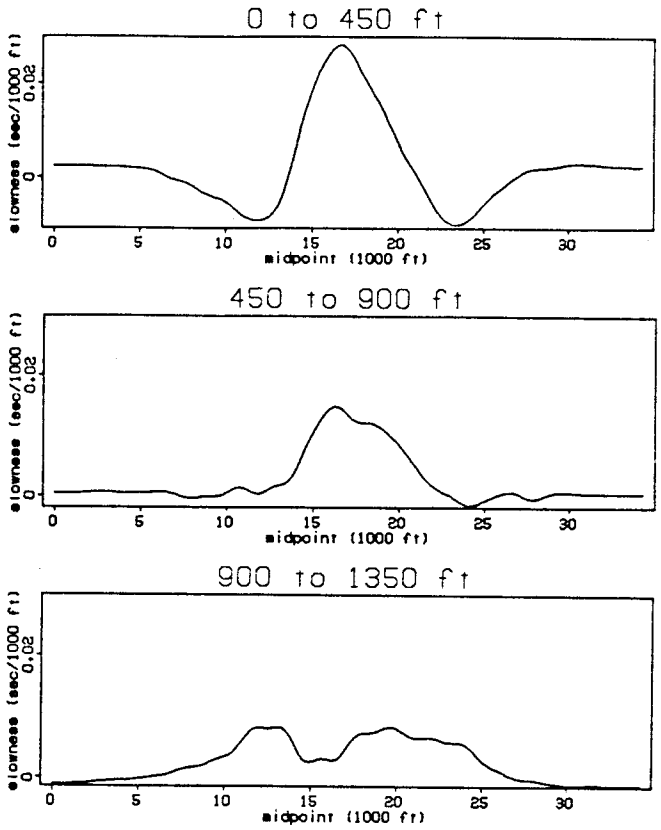

FIG. 7. Cross section through shallowest three layers of model in figure 6.

Figure 7 shows cross sections through the shallowest three layers of the interval slowness model. These three contain most of the anomaly. Now further features are evident. The magnitude of the anomaly is about 12% (i.e. $\frac{\Delta w}{w} = \frac{.02\ sec/1000ft}{.16\ sec/1000ft} = .125$). The negative lobes to either side of the anomaly in the shallowest layer, have corresponding positive lobes on the anomaly in the third layer. The cancellation is not exact; indeed an interesting detail is the way the entire anomaly broadens to the right with depth.

To further investigate the vertical resolution, I tried a second model that had only three anomalous layers. Thus, the entire zone above the shallower reflector was considered to be one layer. Figure 8 shows the inversion results, again using 7% damping. The main features are clearly the same as in the nine-layer model: the anomaly has positive slowness, and is largely confined to the zone above the shallower reflector.

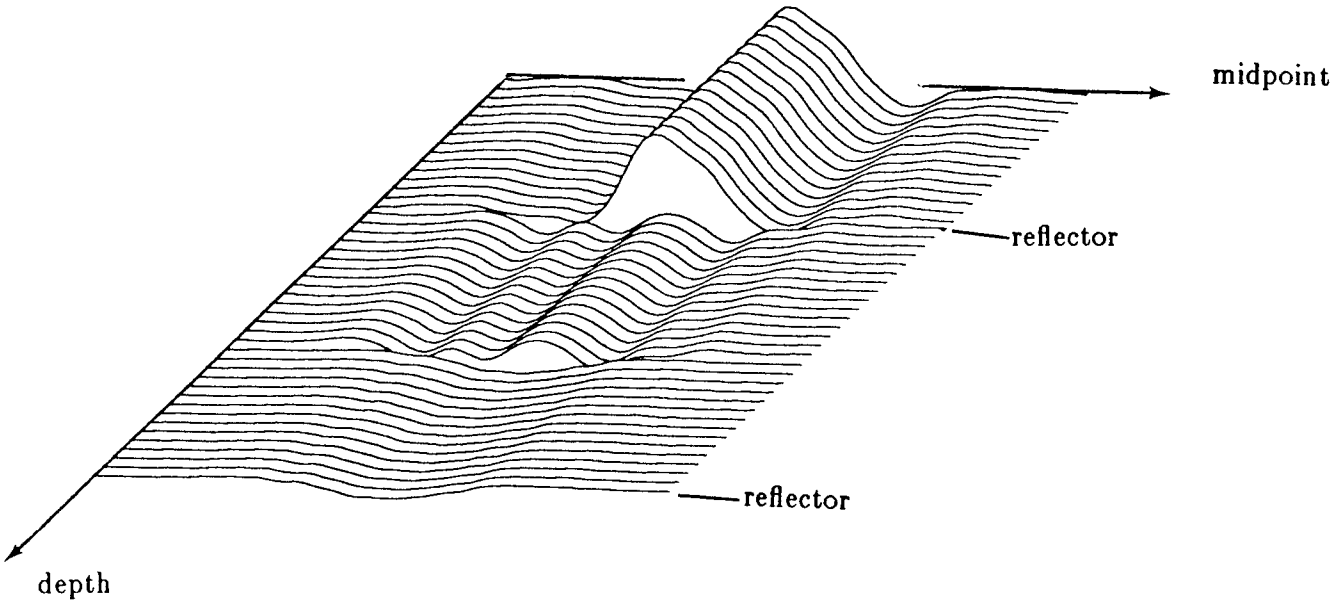

FIG. 8. Anomalous interval slowness model, derived for three layer model. For display purposes the slowness in each layer is repeated fifteen times; thus the discrete nature of the model in depth is clear.

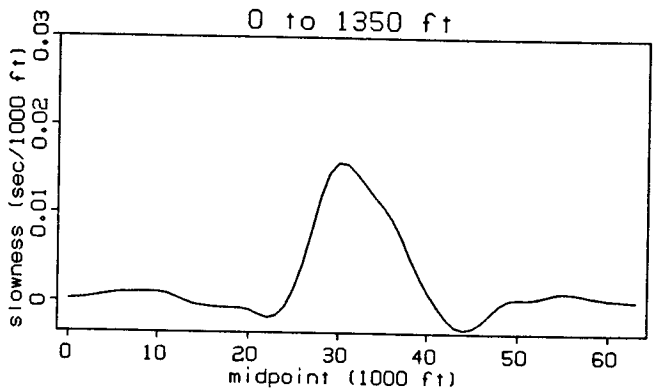

FIG. 9. Cross section through shallowest layer of model in figure 8.

The cross section shown in figure 9 emphasizes the lack of sidelobes. Note that the rightward skew that was visible in figure 7 has produced the asymmetry of the anomaly seen in figure 9. Thus, there is a clear trade-off between resolution of details in the model and overall reliability of the results.

REMOVING EFFECTS OF VELOCITY PERTURBATIONS

Theory

The final portion of the paper seeks to validate the models derived in the previous section. The method used in this paper is based on a decomposition of the interval-velocity distribution into two parts: a laterally invariant background and a laterally varying perturbation. Thus, removing the traveltime effects of the calculated perturbation should leave data that have laterally invariant velocities.

Fermat's principle provides the means for calculating traveltime perturbations due to a perturbation in interval slowness (Δw_{in}). It states that the perturbation in traveltime is just the integral of the anomalous slowness, along the raypaths determined by the background velocity. That is:

$$\Delta t \approx \int_{S_0} \Delta w_{in}\, dS_0$$

where S_0 represents the ray corresponding to the background velocity.

For the flat reflectors and laterally invariant background used here, the background raypaths are easily calculated. From figure 10:

$$\Delta t(y, h, z_r, z_{an}) = \left[\Delta w_{in}\left(y-\frac{x}{2}, z_{an}\right)+\Delta w_{in}\left(y+\frac{x}{2}, za\right)\right]\frac{dz_{an}}{\cos\theta} \tag{7}$$

As shown in figure 10, x and θ depend on the background raypath. This dependence can be expressed by means of the ray parameter ($p = \frac{\sin\theta}{v}$). Specifically,

$$\cos\theta(h, z_r, z_{an}) = \frac{pv(z_{an})}{\left[1-p^2v^2(z_{an})\right]^{1/2}} \tag{8}$$

and

$$x(h, z_r, z_{an}) = 2\int_{z_{an}}^{z_r}\left[1-p^2v^2(z)\right]^{1/2} dz \tag{9}$$

For a constant velocity background, equations (8) and (9) take the much simpler form:

$$\cos\theta = \frac{z_r}{\left[h^2+z_r^2\right]^{1/2}}$$

and

$$x = 2h\,\frac{(z_r-z_{an})}{z_r}$$

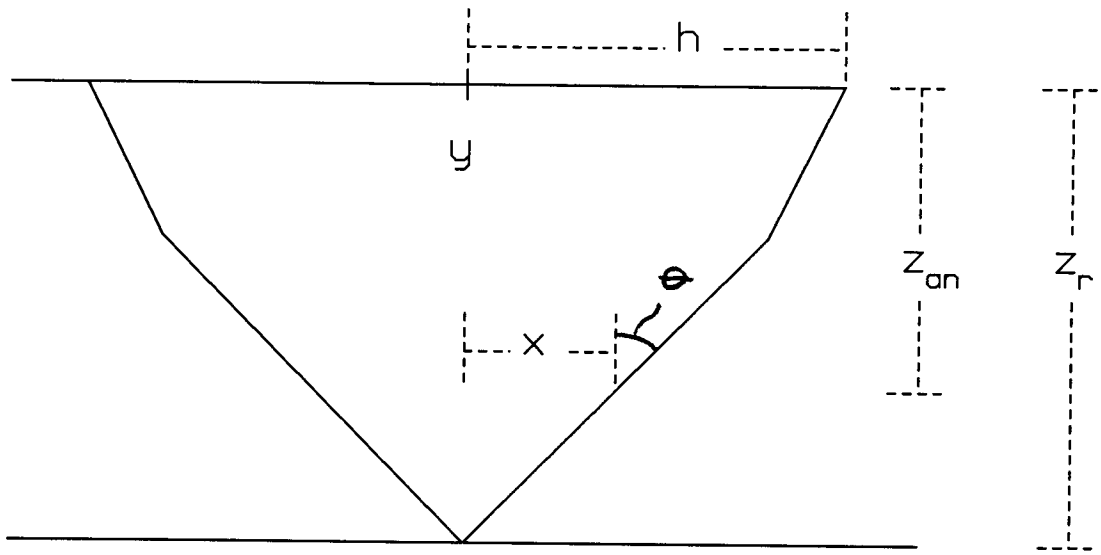

FIG. 10. Diagram of the raypaths to the reflector at depth z_r, for half offset h. The raypath is drawn for a depth variable velocity.

Accumulating the effects from the entire raypath leads to

$$\Delta t(y,h,z_r) = \int_0^{z_r} \left[\Delta w_{in}(y-\frac{x}{2},z_{an}) + \Delta w_{in}(y+\frac{x}{2},za) \right] \frac{dz_{an}}{\cos\theta} \tag{10}$$

Equation (10) can be Fourier transformed over midpoint to produce:

$$\Delta t(k_y,h,z_r) = \int_0^{z_r} \Delta w_{in}(k_y,z_{an}) \cos k_y x \frac{dz_{an}}{\cos\theta} \tag{11}$$

Introducing the Fourier transform of Δw_{in} has simplified the integral. More importantly, equation (11) now expresses the model specifically in terms of the parameters of the inversion: thin strips in depth and sinusoids laterally. Thus the evaluation of equation (11), followed by an inverse Fourier transform over midpoint wavenumber leads to the traveltime perturbations corresponding to the anomalous interval slownesses.

Static shifts

A special case of equation (10) - static shifts - provides an interesting first check of the results. Because the maximum offset is limited, the raypaths for the deep reflectors have a steep propagation angle. Refraction in the low-velocity near surface further steepens these raypaths. Because of the shallowness of the anomalous material, the bulk of the traveltime delay for the deep reflectors will take the form of static shifts.

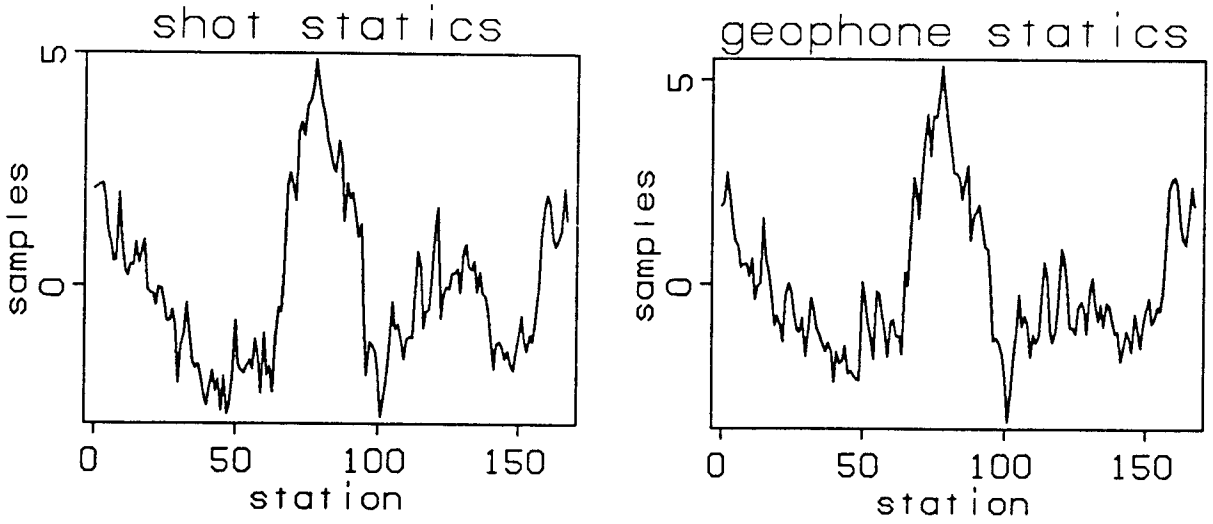

FIG. 11. Shot and geophone statics derived from residual statics program (Ronen).

Figure 11 shows the shot and geophone statics derived from Shuki Ronen's residual statics program (Ronen, 1984). The time gate went from 3.5 to 4 seconds; thus, the statics were determined from the part of the data that best satisfied the conditions needed for vertical raypaths in the near surface. The long wavelength component of these statics can be compared with the traveltime delays predicted by the near surface (i.e. the layers above the first reflector) of the nine layer model, if vertical raypaths are assumed ($\Delta t = \Delta w_{in}\, z$). As shown in figure 12, the comparison is quite good. This suggests that the magnitude and lateral extent of the derived anomaly is quite reasonable.

Figure 13 shows stacked sections of the data, with and without the static corrections of figure 11. The deep portion of the data has clearly been properly corrected for the near-surface anomaly. In the shallower parts, the time sag is still visible and the

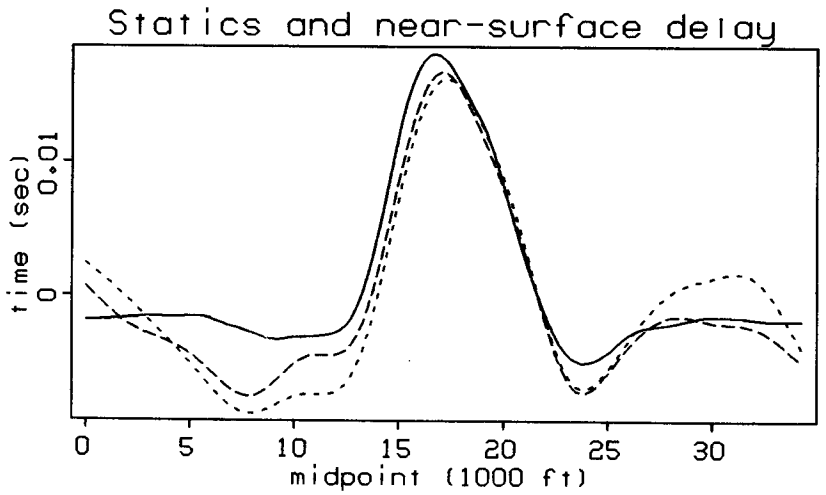

FIG. 12. Comparison between long wavelength component of shot and geophone statics of figure 11 (dashed lines), and near-surface delay predicted by interval slowness model (solid line), based on vertical raypaths in near surface.

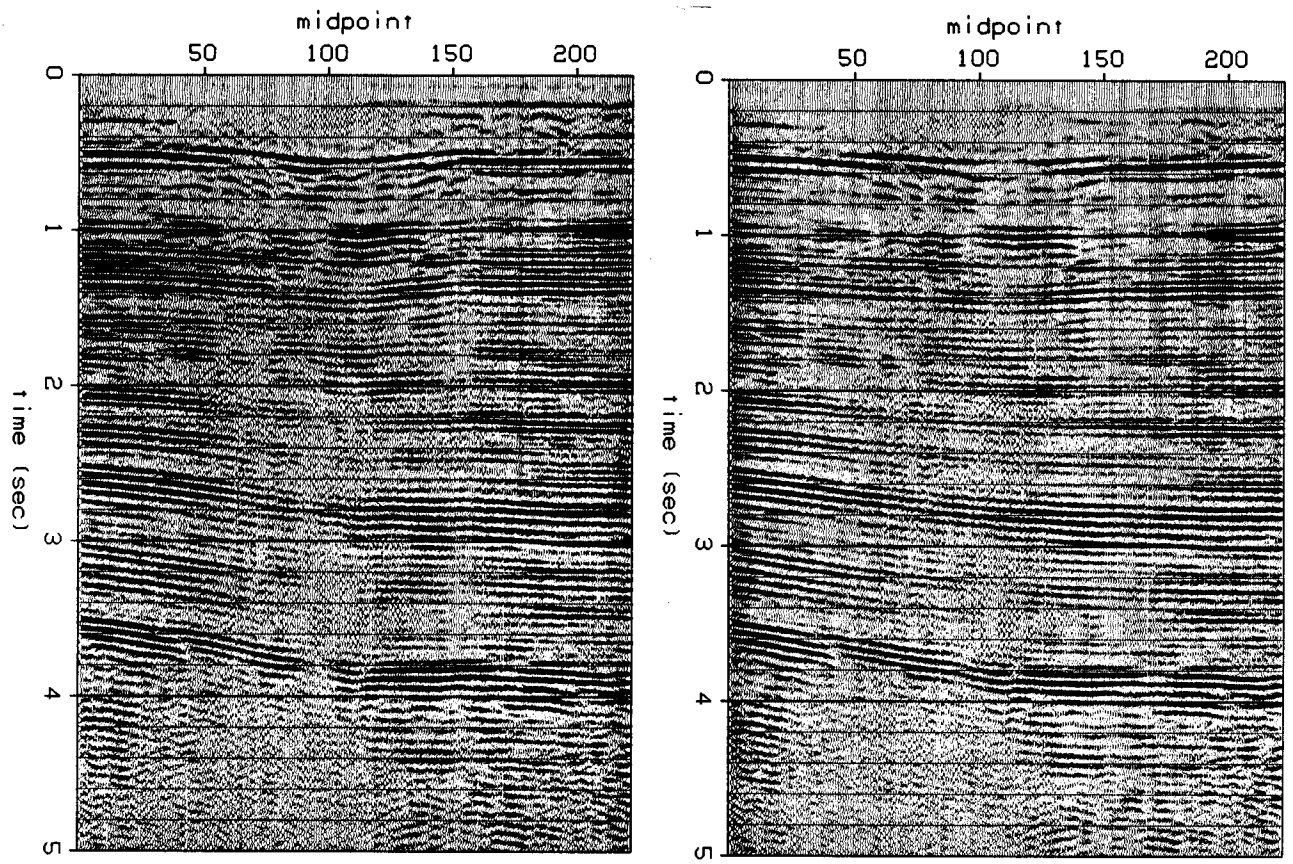

FIG. 13. a) stack without static corrections. b) stack with static corrections.

coherence of the stack imperfect.

Dynamic corrections applied

The more complete offset dependence of equation (11) is required to fully remove the effects of the time sag. Furthermore, the offset dependence provides the connection to depth resolution of the anomaly. In particular, integrating along vertical raypaths through the three-layer and the nine-layer models produces nearly indistinguishable traveltime effects.

Figures 14 show three versions of the same constant-offset section: 14a, 14b, and 14c are respectively uncorrected, statically corrected, and dynamically corrected (i.e. using equation (11), with the anomalous interval slowness of the shallow layers of the nine-layer model). The time sag is quite dramatic in the uncorrected data, and has been effectively removed by both the static and the dynamic corrections. For the small offset used here (1000 ft.), the raypaths are nearly vertical in the near-surface: thus the static and dynamically corrected sections (14b and 14c) should be similar.

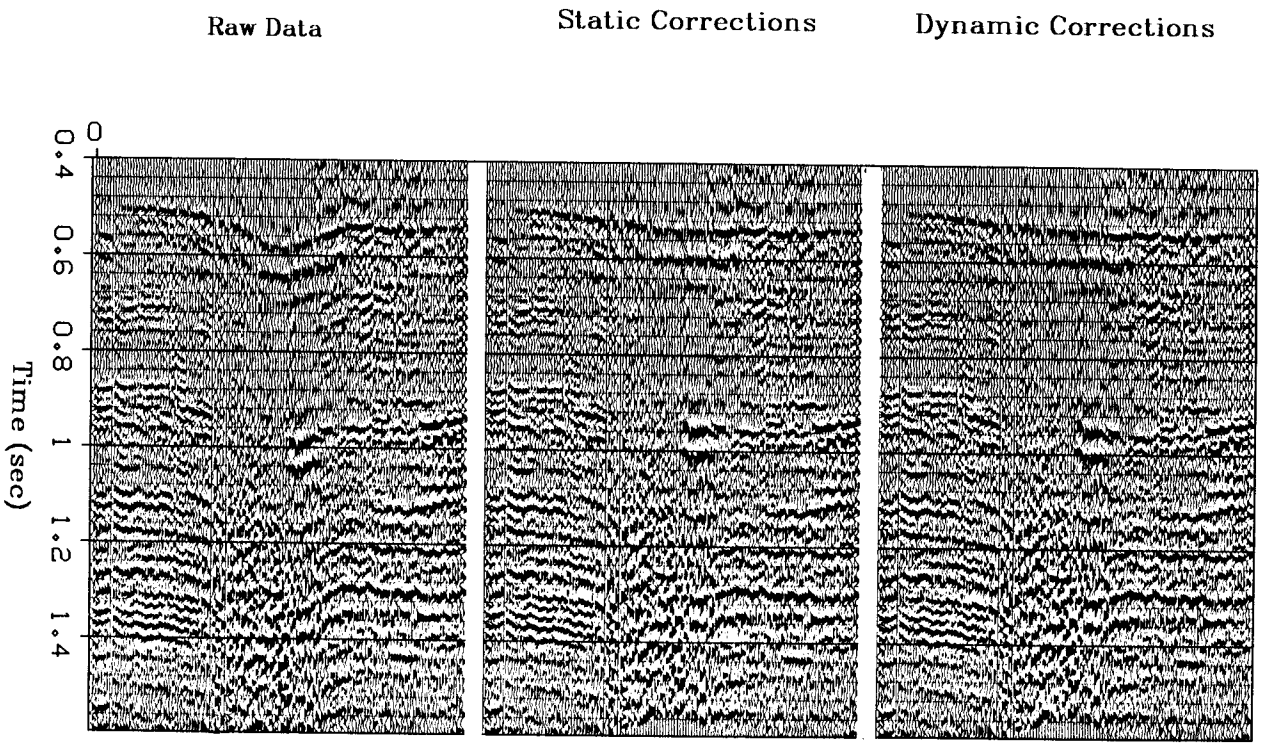

FIG. 14. Near-offset sections for offset = 1000 feet. a) uncorrected. b) statically corrected. c) dynamically corrected.

Figures 15 and 16 make the same type of comparison as figure 14, only now for offsets of 2000 and 3000 ft. respectively. As the offset increases, dynamic corrections become more important. Thus, in figure 16 - the large offset case - only the dynamic corrections have been able to remove the time sag.

These effects are summarized by looking at the stacked section after corrections. Figure 17 shows the stacked sections for uncorrected, statically corrected, and dynamically corrected data. In all cases the data were stacked using one NMO velocity function for the entire line. Once again, the deep portion of the data shows little difference between the static and dynamic corrections. The shallow part shows nearly complete removal of the time sag and good lateral coherence for the dynamically corrected data.

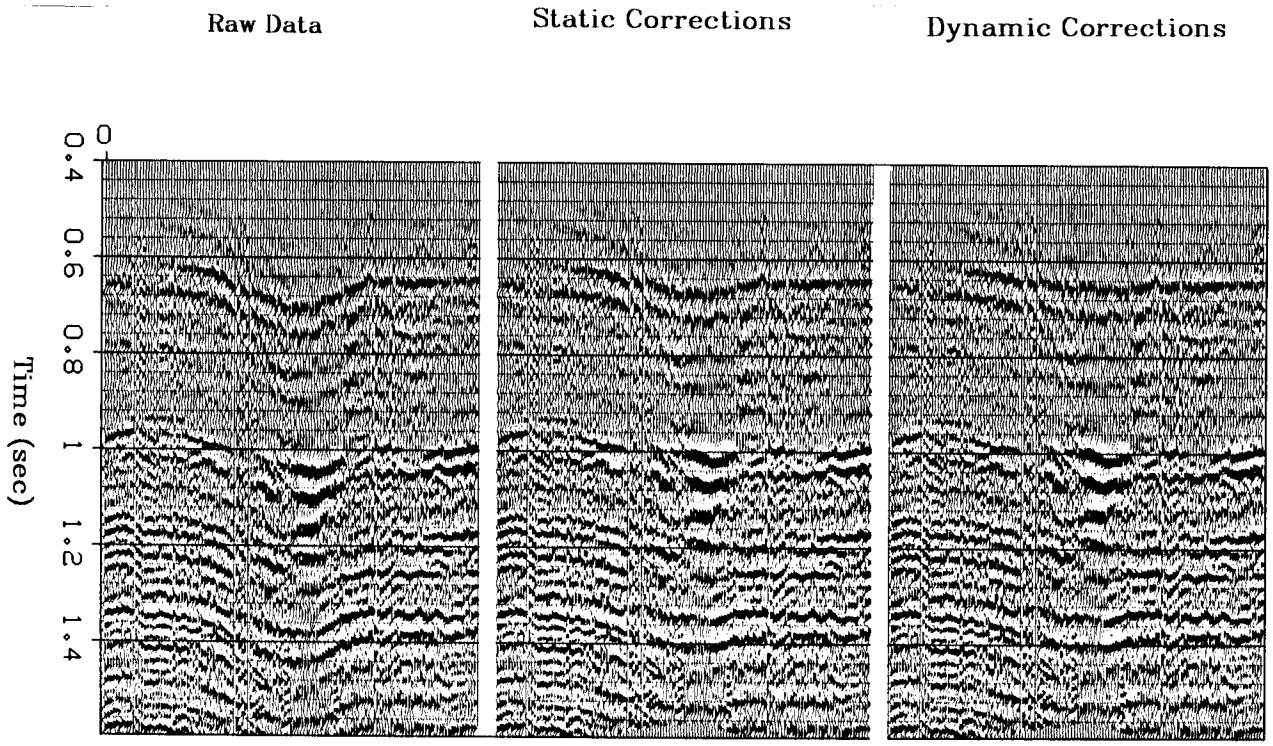

FIG. 15. Near offset sections for offset = 2000 feet. a) uncorrected. b) statically corrected. c) dynamically corrected.

Note that in all of the four previous figures I used only the near-surface portion of the anomalous interval slowness. This was in part because I was interested in comparing the dynamic corrections with the static corrections, which necessarily only involve the near surface. A further reason was that the part of the model between the two reflectors

Raw Data Static Corrections Dynamic Corrections

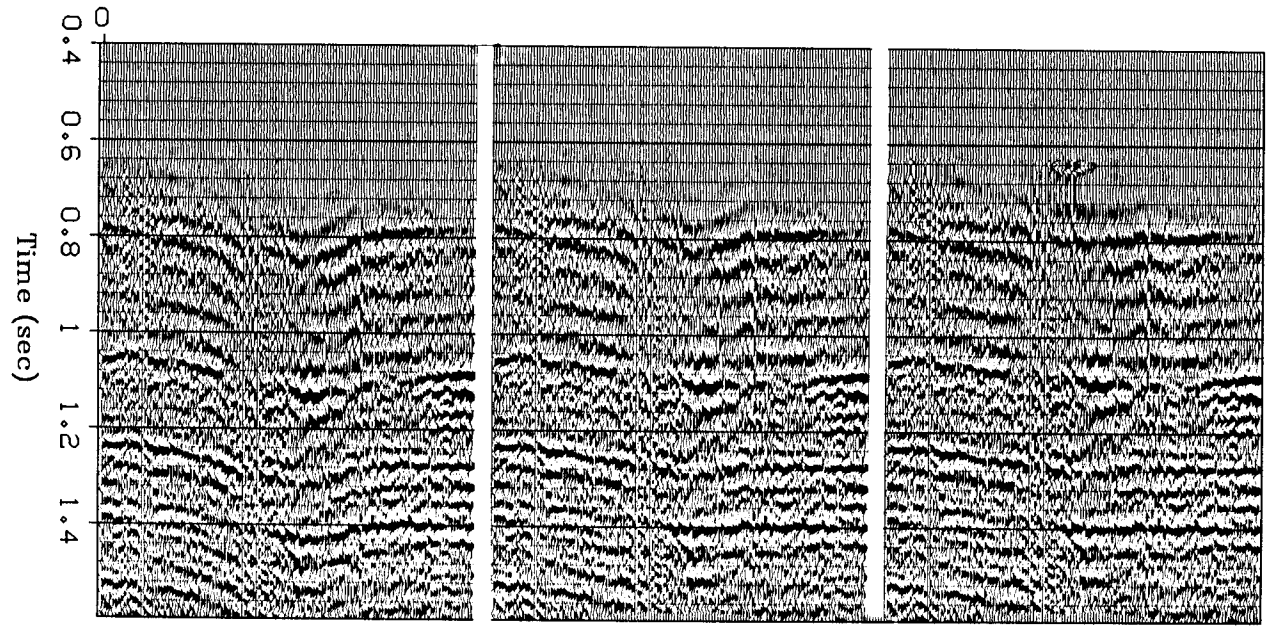

FIG. 16. Near offset sections for offset = 3000 feet. a) uncorrected. b) statically corrected. c) dynamically corrected.

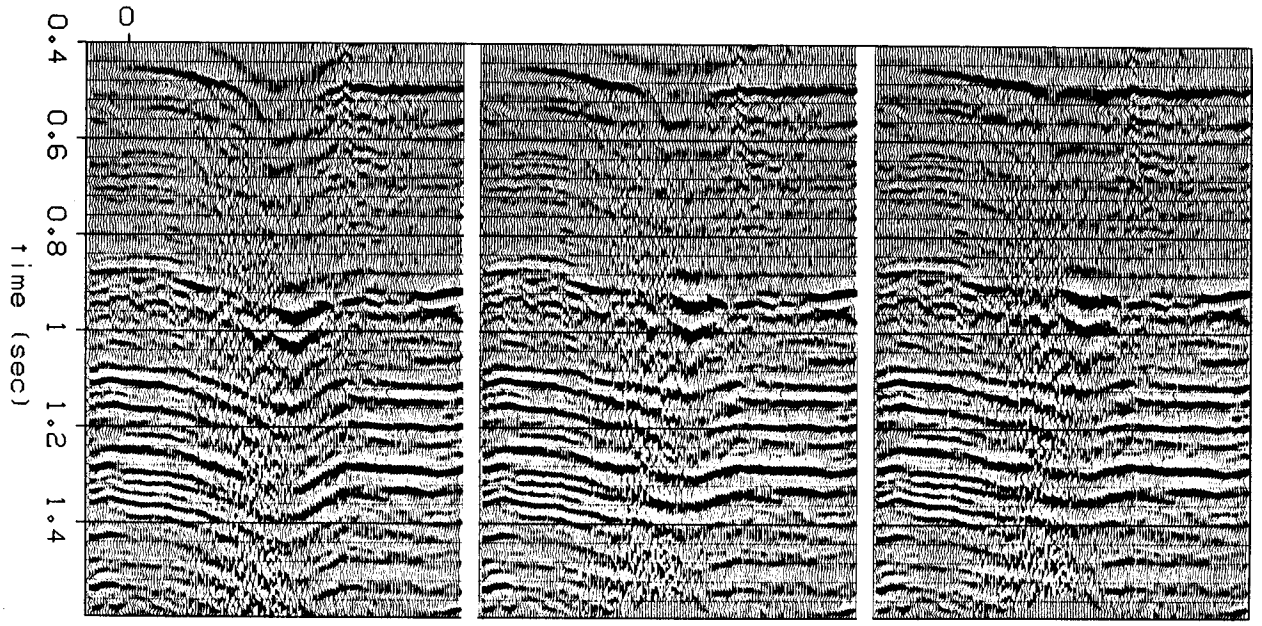

FIG. 17. Sections stacked with one velocity function. a) with no correction for laterally variable velocity, b) with static corrections for laterally variable velocity, c) with dynamic corrections for laterally variable velocity.

was poorly constrained.

Below the shallower reflector the inversion sees data coming only from the deeper reflector; the model in this deeper zone is effectively determined by a single-reflector inversion. Thus, the deeper portion of the models shown in figures 6 and 8 has artifacts associated with the zeroes of the stacking slowness filter. This is unlike the multi-reflector inversion, in which the zeroes of the response from one reflector correspond to different components than do the zeroes from another reflector.

Thus, the details of the inversion results for the part of the model between the reflectors were dominated by inversion artifacts. As a consequence, only a part, albeit the most significant part, of the full traveltime anomaly for the deeper reflectors was removed. This provides a possible explanation for the residual time sag on the deeper reflectors shown in figures 14 through 17.

The differences between the traveltimes predicted by the three-layer and the nine-layer models will be greatest for large offsets. Thus, figure 18 makes this comparison for a constant-offset section with an offset of 3000 feet. The section on the left has used the corrections predicted by the three-layer model, the section on the right the nine-layer model. The differences are subtle, but visible on close inspection.

The shallowest reflector for the three-layer model seems to have produced a slight pull-up in the center of the anomaly. This can be understood as being the result of the large-offset raypaths sensing excessive low-velocity material immediately above the shallow reflector. The nine-layer model has no such problem; because the anomaly decreases with depth, the large-offset rays actually undershoot the main body of the anomaly.

These differences are indeed subtle ones; they are visible only at the large offset reflections from the shallow section. Nonetheless, the conclusion is a familiar one for inverse problems: one must choose between a result that better explains the data (the nine-layer model) and a result that is more interpretable (the three-layer model).

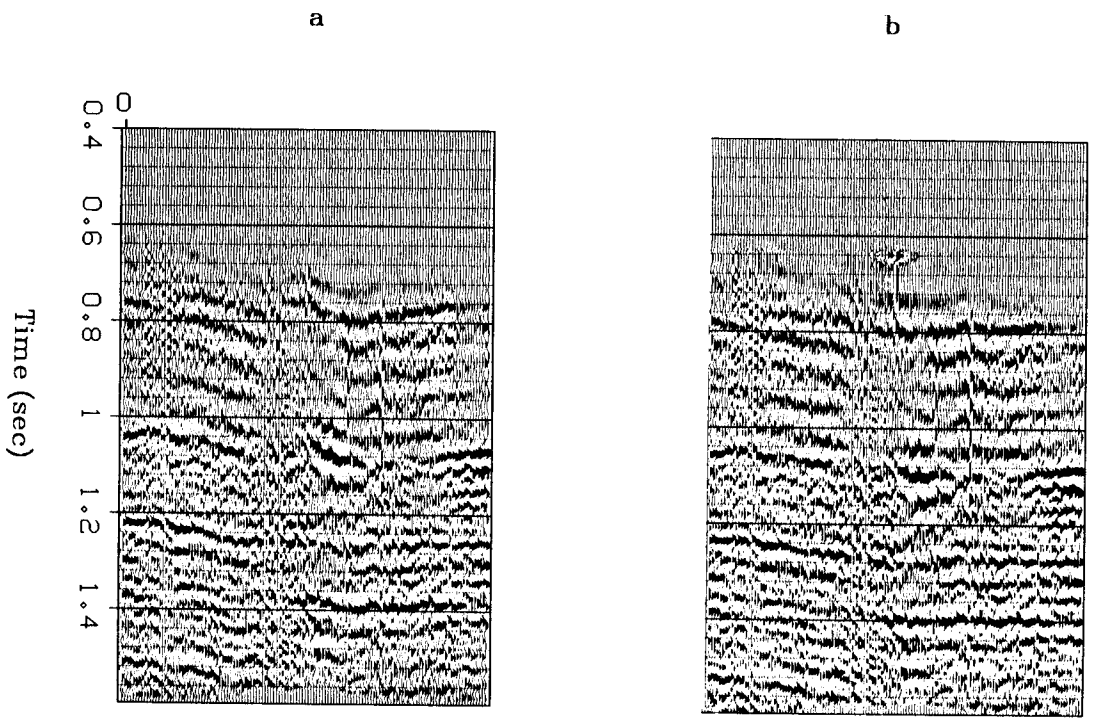

FIG. 18. Constant-offset section at offset = 3000 feet. a) dynamic corrections based on three-layer model. b) dynamic corrections based on nine-layer model.

Velocity analysis

A second velocity analysis, performed after the anomalous-traveltime corrections, provides a final and very revealing way of looking at the results. After all, the basic idea was to separate the velocities into a laterally variable and a laterally invariant part. The traveltime corrections were aimed at removing the laterally variable part, so presumably, a velocity analysis after corrections should result in laterally invariant velocities.

A conventional velocity analysis provides semblance as a function of zero-offset time, midpoint and stacking velocity (or slowness). Because a flat reflector has an approximately constant zero-offset time, its contribution to the semblance analysis will lie in a few consecutive time planes. Thus, a time average of these planes will provide semblance as a function of midpoint and velocity for this reflector, that is a horizon velocity analysis (see figure 19).

Figure 20 shows the plane at 1.35 seconds, i.e. the deeper reflector used in the inversion. As with the constant offset sections, I show three cases: uncorrected, statically

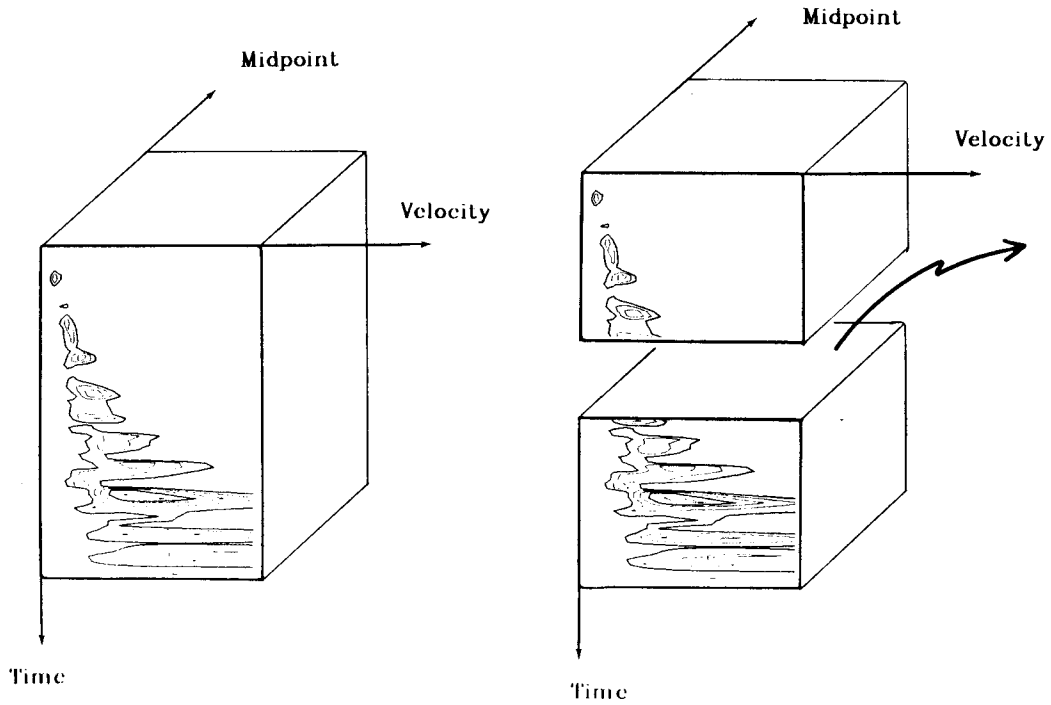

FIG. 19. A conventional velocity analysis provides semblance as a function of zero-offset time, midpoint and stacking velocity (or slowness). For flat reflectors, a time slice of this cube is a simple horizon velocity analysis.

corrected, and dynamically corrected. The uncorrected velocity analysis is exactly the one I picked to get my original Δw_s. The corrected data (both static and dynamic) show a velocity analysis with little lateral variation. Thus, exactly as with the traveltimes, the derived interval slowness model provides a good explanation of the lateral variation in stacking slowness. Figure 21 is analogous to figure 20, only for the shallower reflector. Now the deficiencies of the static corrections are clear: only the dynamic corrections result in a laterally-invariant velocity analysis.

CONCLUSIONS

This paper has looked in detail at a field dataset with laterally-varying velocities. The analysis was based on the inversion of stacking velocity anomalies to interval velocity anomalies. Although the stacking velocities for reflectors at all depths showed strong lateral variation, the inversion produced an interval velocity model with lateral variation only in the shallowest layers. This model was able to explain most of the

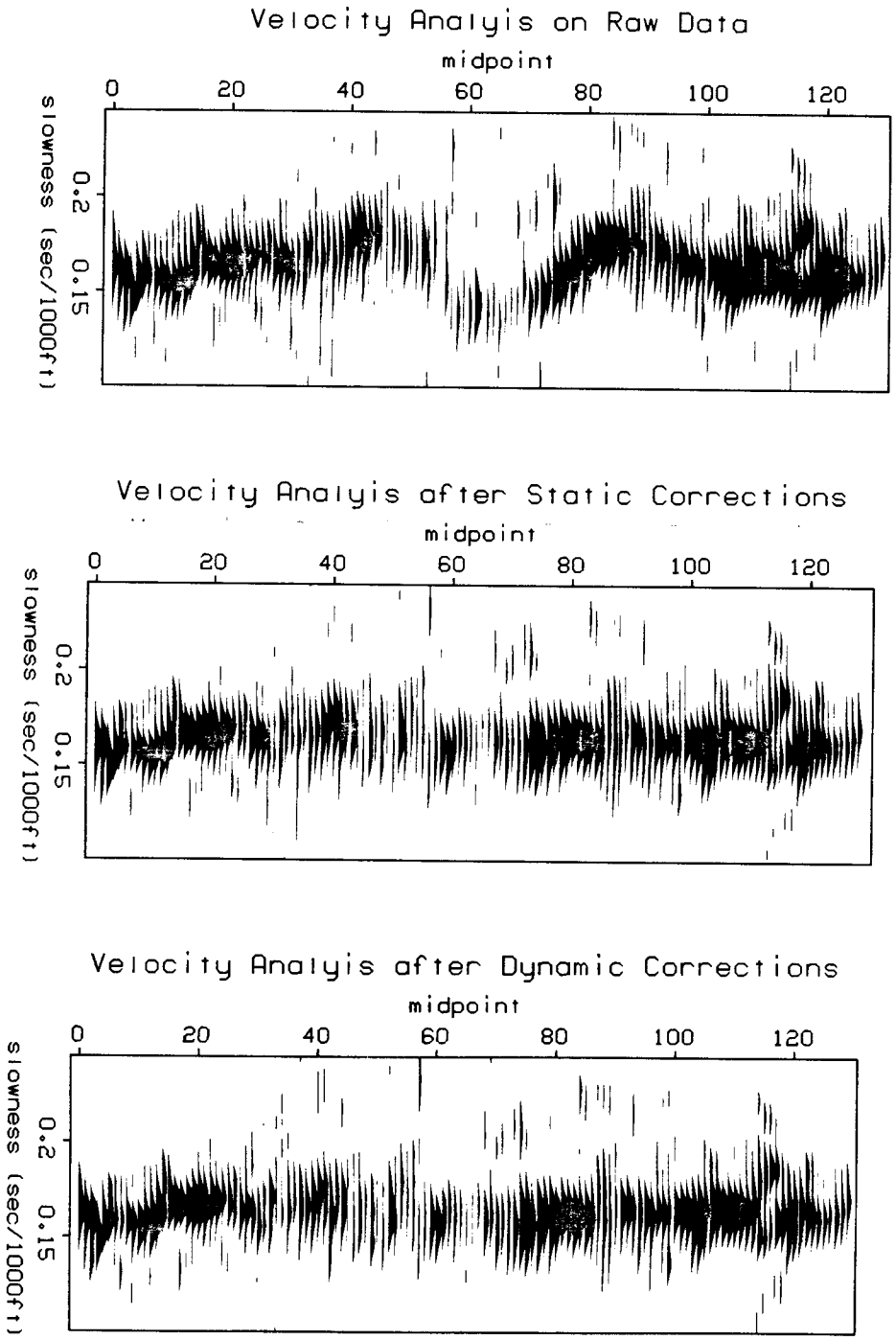

FIG. 20. Velocity analysis for reflector at 1.35 seconds, a) with no near-surface corrections, b) after static near-surface corrections, c) after dynamic near-surface corrections.

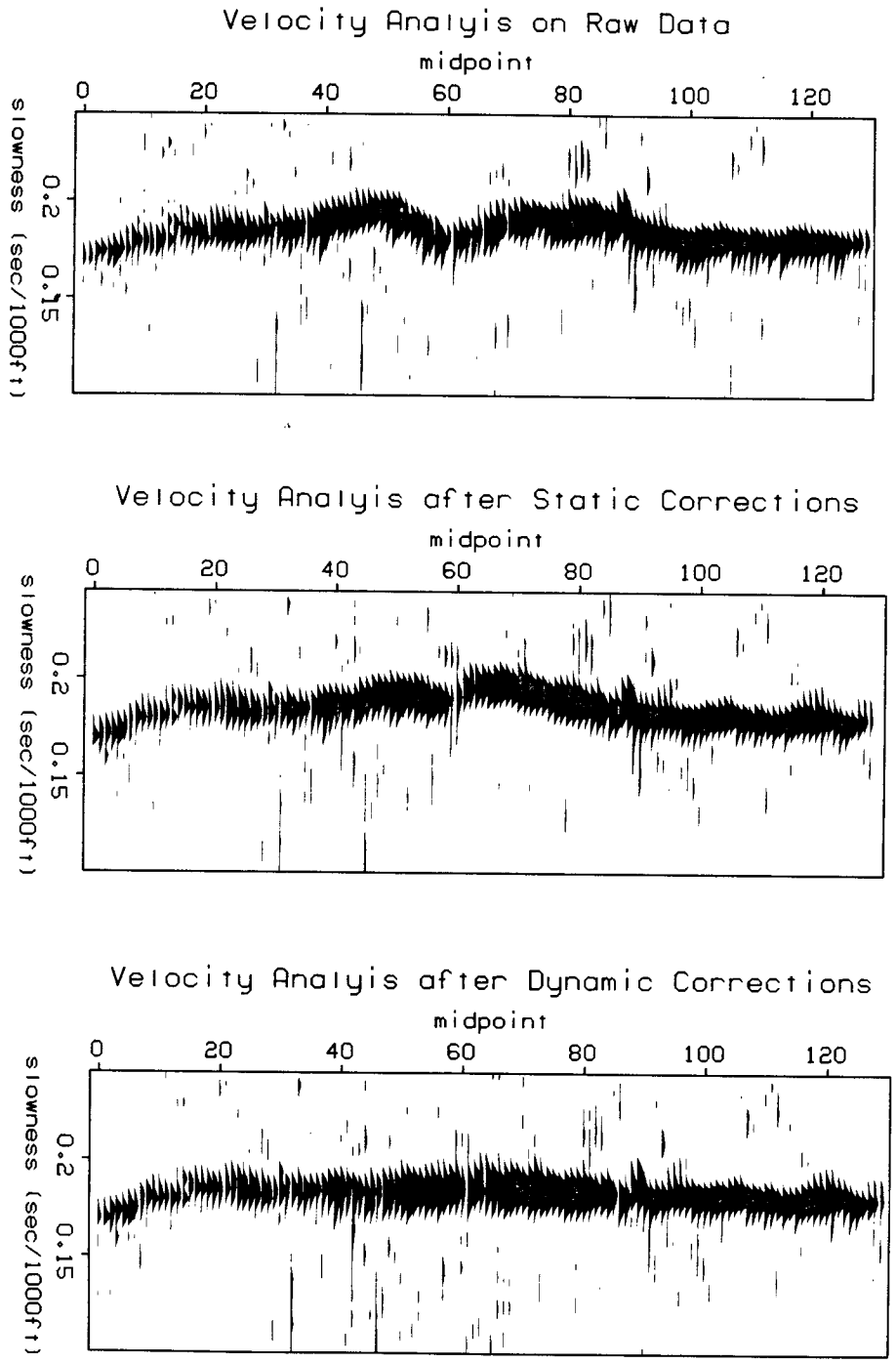

FIG. 21. Velocity analysis for reflector at .5 seconds, a) with no near-surface corrections, b) after static near-surface corrections, c) after dynamic near-surface corrections.

lateral variation in the traveltimes.

ACKNOWLEDGMENTS

I wish to thank Bill Ostrander of Chevron USA for providing the data that I used in this paper. I also thank Shuki Ronen for help with his residual statics program.

REFERENCES

Loinger, E., 1983, A linear model for velocity anomalies, Geophysical Prospecting, v.31, p.98-118.

Rocca, F. and Toldi, J., 1982, Lateral velocity anomalies: SEP-32, p.1-13.

Ronen, J., 1984, Surface-consistent residual statics by stack optimization: SEP-38, p.27-38.

Toldi, J., 1984, Resolution of interval velocities from stacking velocity anomalies: SEP-38, p.89-104.

Toldi, J., 1984, Velocity analysis without picking: SEP-41, (this report)